




Impact of Horizontal Model Resolution on Mixing and Dispersion in the Northeastern Gulf of Mexico

 Nektaria Ntaganou¹ , Eric P. Chassignet¹ , and Alexandra Bozec¹ 
¹Center for Ocean-Atmospheric Prediction Studies (COAPS), Florida State University, Tallahassee, FL, USA

Key Points:

- Resolving submesoscale motions leads to increased Lagrangian transport and mixing as well as the generation of more intricate LCSs
- Chaotic advection dominates turbulent mixing regardless of the horizontal model resolution (either 4 km or 1 km)
- Submesoscale-permitting simulation yields reduced error against drifter observations compared to mesoscale-resolving counterpart

Supporting Information:

Supporting Information may be found in the online version of this article.

Correspondence to:

 N. Ntaganou,
mntaganou@fsu.edu
Citation:

 Ntaganou, N., Chassignet, E. P., & Bozec, A. (2024). Impact of horizontal model resolution on mixing and dispersion in the northeastern Gulf of Mexico. *Journal of Geophysical Research: Oceans*, 129, e2024JC021315. <https://doi.org/10.1029/2024JC021315>

Received 14 MAY 2024

Accepted 22 OCT 2024

Author Contributions:

Conceptualization: Nektaria Ntaganou, Eric P. Chassignet
Data curation: Alexandra Bozec
Formal analysis: Nektaria Ntaganou
Funding acquisition: Eric P. Chassignet
Investigation: Nektaria Ntaganou
Methodology: Nektaria Ntaganou
Project administration: Eric P. Chassignet
Resources: Eric P. Chassignet
Software: Alexandra Bozec
Supervision: Eric P. Chassignet
Validation: Nektaria Ntaganou
Visualization: Nektaria Ntaganou
Writing – original draft: Nektaria Ntaganou
Writing – review & editing: Nektaria Ntaganou, Eric P. Chassignet

© 2024. The Author(s).

 This is an open access article under the terms of the [Creative Commons Attribution License](https://creativecommons.org/licenses/by/4.0/), which permits use, distribution and reproduction in any medium, provided the original work is properly cited.

Abstract In this paper, the importance of model horizontal resolution in mixing and dispersion is investigated by comparing two data-assimilative high-resolution simulations (4 and 1 km), one of which is submesoscale-permitting. By employing both Eulerian and Lagrangian metrics, upper-ocean differences between the mesoscale-resolving and submesoscale-permitting simulations are examined in the northeastern Gulf of Mexico, a region of high mesoscale and submesoscale activity. Mixing in both simulations is explored by conducting Lagrangian experiments to track the generation of Lagrangian coherent structures (LCSs) and their associated transport barriers. Finite-time Lyapunov exponent (FTLE) fields show higher separation rates of fluid particles in the submesoscale-permitting case, which indicate more vigorous mixing with differences being more pronounced in the shelf regions (depths ≤ 500 m). The extent of the mixing homogeneity is examined using probability density functions (PDFs) of FTLEs with results suggesting that mixing is heterogeneous in both simulations, but some homogeneity is exhibited in the submesoscale-permitting case. The FTLE fields also indicate that chaotic advection dominates turbulent mixing in both simulations regardless of the horizontal resolution. In the submesoscale-permitting experiment, however, smaller scale LCSs emerge as noise-like filaments that suggest a larger turbulent mixing component than in the mesoscale-resolving experiment. The impact of resolution is then explored by investigating the spread of oil particles at the location of the Deepwater Horizon oil spill.

Plain Language Summary Small-scale processes (0.1–50 km) play a critical role in upper-ocean water transport and mixing. Thus, the added value from resolving these finer scales in numerical models is evaluated by comparing two high-resolution numerical simulations in the northeastern Gulf of Mexico: one at 1 km horizontal resolution that truly resolves features on the order of 10 km and one at 4 km that only resolves features greater than 50 km. Passive fluid particle experiments are conducted to document the mixing and identify structures that act as barriers to transport between fluids with different properties and determine the fate of dispersants in the ocean. In both simulations, the particles' distribution is spatially heterogeneous, which indicates that mixing is largely controlled by these structures. Results also show that neighboring fluid particles separate faster from one another in the 1 km simulation than in the 4 km simulation, meaning that mixing of fluids is more intense. Lastly, we find that the 1 km simulation is more realistic when applied to oil particle dispersion at the location of the Deepwater Horizon oil spill.

1. Introduction

Beron-Vera (2010) investigated the impact of resolution on Lagrangian transport by mesoscale features by comparing $1/4^\circ$ altimetry-derived geostrophic velocity data in the Antarctic Circumpolar Current (ACC) to model data at $1/12^\circ$ horizontal resolution. He argued that higher resolution is essential to further understand the nature of mixing and perform deterministic calculations of Lagrangian transport in highly energetic eddy-rich regions in the ocean. Specifically, Beron-Vera (2010) showed that the mixing was heterogeneous in both data sets, implying that chaotic advection dominates over turbulent mixing with more intricate coherent structures being revealed with the increase of resolution. Furthermore, submesoscale processes (0.1–50 km, Callies et al. (2015); McWilliams (2016)), with Rossby number of $O(1)$ ($R_o = \frac{U}{Lf}$, where U is the characteristic flow velocity, L is the spatial scale of the feature, and f is the Coriolis parameter) have been shown to be crucial in understanding upper ocean dynamics (McWilliams, 2016) with respect to transport of tracers and mixing (Capet et al., 2008a; Thomas et al., 2008). With advancements in numerical model resolution as well as increase in observational data availability, these finer-scale processes have been increasingly studied either solely (Mahadevan & Tandon, 2006; Thomas et al., 2008) or in relation to coexisting mesoscale processes (Capet et al., 2008b, 2008c; Liu et al., 2018, 2021; Yang et al., 2021). The importance of understanding the influence of submesoscale dynamics

on the larger picture of the mesoscale lies on the fact that one cannot exist without the other. One cannot differentiate where submesoscale ends and where mesoscale begins.

The impact of the submesoscale on Lagrangian transport in the Gulf of Mexico (GoM) was studied by Zhong and Bracco (2013) by comparing a submesoscale-permitting simulation (~1 km horizontal resolution) to a mesoscale-resolving one (~5 km horizontal resolution). They showed that the submesoscale-permitting simulation revealed energetic filaments and accumulation zones due to ageostrophic processes that were not present in the mesoscale-resolving one. Increased submesoscale-permitting horizontal resolution has also been shown to be important for biochemical processes that are better understood with the inclusion of small-scale structures, which accompany the larger mesoscale features (Zhong & Bracco, 2013). Submesoscale-permitting simulations also result in larger vertical velocities in the mixed layer as well as higher rates of vertical mixing in the northern and western GoM (Liu et al., 2021; Zhong & Bracco, 2013).

In the present study, we aim to further investigate the value added from resolving those finer scales with respect to Lagrangian transport and mixing. Specifically, we address the question as to whether chaotic advection still dominates turbulent mixing as in Beron-Vera (2010) or if turbulent mixing becomes more important when submesoscale features are resolved. We define mixing as the process of irreversibly altering the properties of fluids (such as temperature and salinity) that interact with one another at different scales. Chaotic advection refers to mixing induced by stretching and folding of chaotic flows, essentially the component of mixing determined by coherent structures, that are organized structures that act as transport barriers (Aref, 1984; Aref et al., 2017). Turbulent mixing, on the other hand, is driven by turbulent fluid motions that eliminate gradients almost instantaneously. Turbulent motions are the result of energy cascading from large to small scales through a large Reynolds number input. Chaotic advection is a kinematic effect, meaning that high Reynolds numbers, thus high inputs of energy, are not necessary (Aref et al., 2017). Chaotic advection is predominantly controlled by quasi-regular flows and coherent structures/filaments and characterized by spatial inhomogeneity of particle dispersion or finite-time Lyapunov exponent (FTLE) fields. In contrast, turbulent mixing, which is the result of irregular and incoherent flows, is characterized by a spatially homogeneous distribution of fluid particles.

The impact of resolving the submesoscale is quantified by using two data-assimilative simulations at 4 and 1 km horizontal resolutions, respectively. In both simulations, the mesoscale fields are constrained by assimilating the same observational data on the 4 km grid. In the submesoscale-permitting (1 km resolution) simulation, the submesoscale field is, however, allowed to develop and evolve. This is an advantageous set-up, as any differences emerging from the comparison of the two simulations can be directly attributed to the presence of the submesoscale field, since the mesoscale fields are constrained in both simulations. In Zhong and Bracco (2013), their simulations only allowed for a statistical approach of the effects of the submesoscale field on Lagrangian transport. Using Eulerian and Lagrangian metrics, the aim is to elucidate the role of the added resolution on the Lagrangian transport and mixing. We focus on the northeastern GoM, which exhibits high mesoscale and submesoscale activity (Figure 1) and which is known for its biogeochemical importance especially during the DeepWater Horizon oil spill (Beron-Vera & LaCasce, 2016; Liu et al., 2011, 2018; Olascoaga & Haller, 2012; Poje et al., 2014; Zhong & Bracco, 2013). The submesoscale regime often develops around mesoscale eddies and frontal jets in the form of smaller eddies or sharp fronts and filaments (Bracco et al., 2019; D'Asaro et al., 2011; McWilliams, 2016). Submesoscale eddies form primarily due to mixed-layer instabilities (Molemaker et al., 2005) or frontogenesis (Capet et al., 2008c).

The paper is organized as follows: After a brief overview of the model configurations and the data assimilation approach, the added value of the increased resolution between the two numerical simulations is discussed in Section 2 by comparing model surface velocities from both simulations to surface drifter velocities. In the range of the scales that are constrained by the assimilated observations, root mean square errors in velocities between the simulations and observational data sets suggest that the error is reduced when the model resolution is increased in agreement with Jacobs et al. (2019). Differences in kinetic energy spectra between the numerical simulations indicate that the submesoscale-permitting simulation exhibits higher kinetic energy and flatter spectral slopes as shown by Zhong and Bracco (2013). In Section 3, the impact of the increased resolution on the Lagrangian transport and mixing is analyzed by first performing Lagrangian particle experiments forward and backward in time. The forward in time trajectories are used to calculate particle distributions and compute cumulative and total distances covered. The backward in time trajectories are used to calculate FTLEs and their associated attracting Lagrangian coherent structures (LCSs). The FTLE fields and their LCSs show that mixing is more vigorous in the

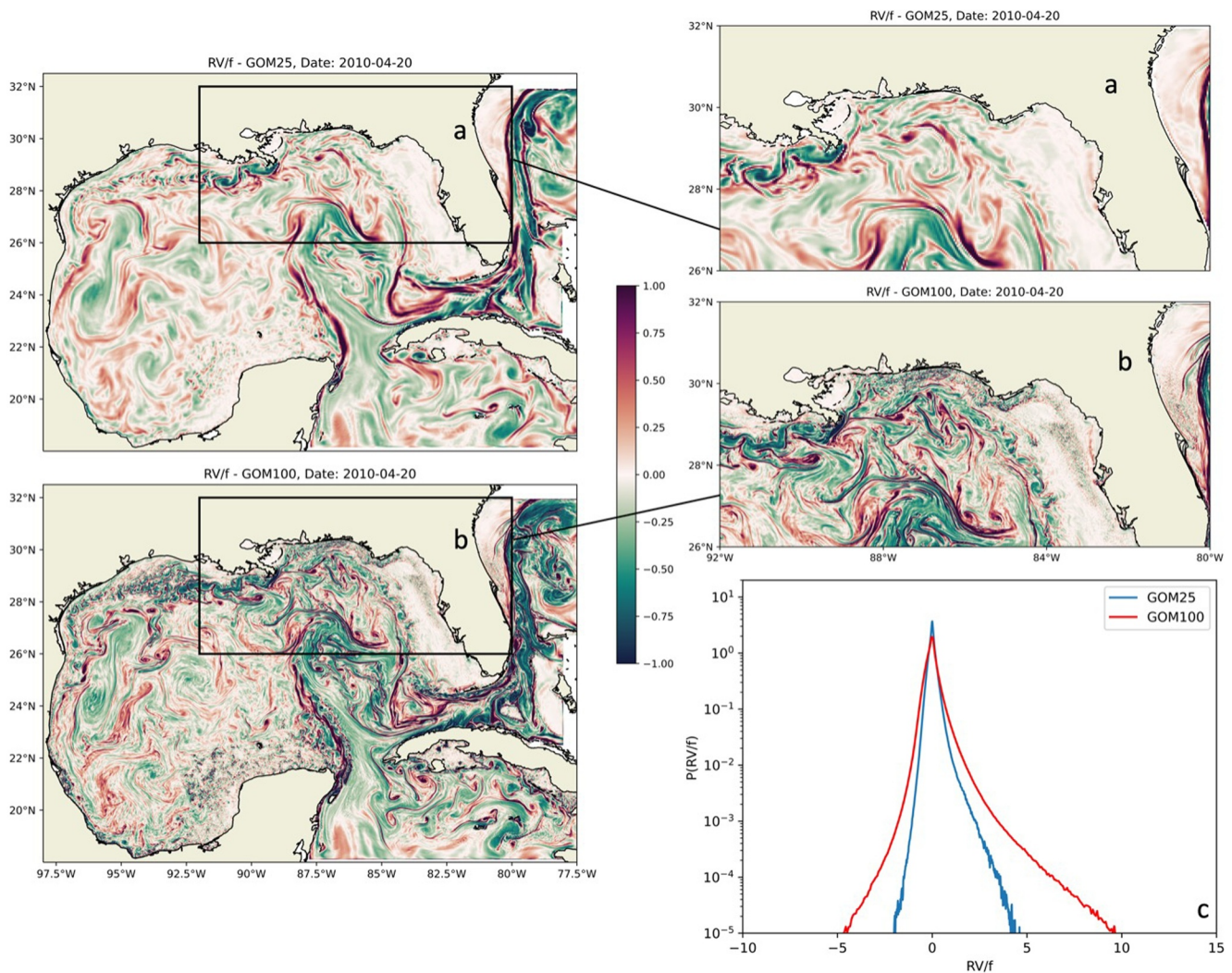


Figure 1. Snapshots of normalized relative vorticity (RV/f) for (a) GOM25 and (b) GOM100 on 20 April 2010. The black box indicates the region of the northeastern GoM where Lagrangian particle experiments were conducted. A magnified version of the region enclosed by the black box in panels (a) and (b) is shown on the right column along with its PDFs of normalized relative vorticity (RV/f) for GOM25 in blue and GOM100 in red. The PDF skewness values are 2.3 for GOM25 and 3.4 for GOM100.

submesoscale-permitting case and the PDFs of FTLEs provide insight on the extent of mixing homogeneity. Similarities in the structure of FTLEs between the simulations suggest that chaotic advection prevails over turbulent mixing and that Lagrangian mixing is to an extent insensitive to resolution as shown by Beron-Vera (2010) for mesoscale flows. Finally, the impact of resolving submesoscale features is discussed in Section 4 in the context of oil particle experiments during the 2010 Deepwater Horizon spill, with more oil particles reaching the northern GoM shelf in the submesoscale-permitting case compared to the mesoscale-resolving one, within the span of a month from the release date. A summary and concluding remarks are presented in Section 5.

2. Eulerian Comparison of the 1/25°- and 1/100°-Resolution Hindcast Simulations

In this section, we compare a subset of two high-resolution 20+ year reanalyses performed with the Hybrid Coordinate Ocean Model (HYCOM) (Bleck, 2002; Chassignet et al., 2003) applied in the GoM at 1/25° (~4 km) and 1/100° (~1 km) horizontal resolution. Details on the numerical model and the hindcasts are provided in Sections 2.1 and 2.2, respectively. To demonstrate the value of the increased resolution, an evaluation of the RMS error in model velocities against surface drifter velocities is conducted in Section 2.3. Finally, in Section 2.4, we discuss the differences in terms of normalized relative vorticity and kinetic energy spectra (Eulerian metrics).

2.1. Numerical Model

The model domain of both configurations extends from 98°E to 77°E in the zonal direction and from 18°N to 32°N in the meridional direction. The vertical resolution consists of 41 hybrid layers. The layers are isobaric in the mixed layer, terrain-following at the continental shelf, and isopycnal in the stratified deep ocean interior (Bleck, 2002). The latest version of the model (2.3.01: <https://github.com/HYCOM/HYCOM-src>) is forced with hourly Climate Forecast System Reanalysis (CFSR) atmospheric fields from 2001 to 2011 and CFSRv2 fields from 2012 onward. The lateral open boundaries are relaxed to daily means of the global HYCOM GOFS3.1 reanalysis (<https://www.hycom.org/dataserver/gofs-3pt1/reanalysis>). Tidal forcing with five tidal constituents (M2, S2, O1, K1, and N2) is applied at the surface through a local tidal potential and at the boundaries with Browning-Kreiss boundary conditions. The tidal data are extracted from the Oregon State University (OSU) TPX09 atlas (Egbert & Erofeeva, 2002). The river discharge data are obtained from a US Navy database and come from a 12-month climatology from 40 rivers in the GoM region. The river forcing is introduced in the model as a surface mass flux distributed over several points around each river mouth. The bathymetry for the 1/25° and 1/100° domains is derived from the high resolution 1 km GoM bathymetry of Velissariou (2014), but for the 1/25° domain, it is interpolated on the 1/25° grid. The horizontal advection uses a second-order flux corrected transport scheme. The horizontal diffusion uses a combination of a Laplacian diffusion of $0.0025\Delta x$ and a biharmonic dissipation of $-0.02\Delta x^3$ for velocities and the same biharmonic diffusion for tracers. An interface height smoothing is applied through a biharmonic operator (with a velocity scale of 0.01 m/s). Finally, the vertical mixing is provided by the KPP model (Large et al., 1994) with a background diffusivity of $10^{-5} \text{ m}^2/\text{s}$.

2.2. Data Assimilation

Both configurations are data-assimilative and the hindcasts are produced with the use of the tendral statistical interpolation (T-SIS) package (Srinivasan et al., 2022). The basic functionality of the package is a multivariate linear statistical estimation given a predicted ocean state and observations. To optimize the system's performance for the HYCOM Arbitrary-Lagrangian-Eulerian (ALE) vertical coordinate system, subsurface profile observations are first remapped onto the model hybrid isopycnic-sigma-pressure vertical coordinate system prior to assimilation. The analysis procedure then updates each coordinate layer separately in a vertically decoupled manner. A layered version of the Cooper and Haines (1996) procedure is used to adjust model layer thicknesses in the isopycnic-coordinate interior in response to SSH anomaly innovations. Prior to calculating SSH innovations, a mean dynamic topography (MDT) derived from a 20-year free-run of the GOMB0.04 configuration is added back into the altimetry observations. The multiscale sequential assimilation scheme based on a simplified ensemble Kalman Filter (Evensen, 2003; Oke et al., 2002) is used to combine the observations and the model to produce the best estimates of the ocean state at analysis time. This state is then inserted incrementally into HYCOM over 9 hr. The analysis is done daily at 18Z.

In the 1/100° configuration, since the resolution of the observations that are fed to the TSIS assimilation system is not high enough compared to the grid resolution, the analysis is performed on the 1/25° grid. The 1/100° ocean state is first box-car averaged at 1/25° to remove the small-scale variability and given to TSIS as the ocean state. The assimilation system then performs the reanalysis at this resolution and provides an increment that is then interpolated back at the 1/100° grid and added to the 1/100° configuration ocean state.

The TSIS assimilative system accepts sea level anomaly (SLA), sea surface temperature (SST), and T/S profiles. For the hindcasts used in the present study, remotely sensed SLA and SST were assimilated as well as in situ T/S, which are considered to be the most reliable observations. Along-track SLA from four operational satellite altimeters (T/P, Jason 1,2, Envisat, GFO, and Cryosat) constitute the most important data set for constraining the model. The data are available from Collecte Localisation Satellites (CLS) from January 1993 to present (<https://www.avisio.altimetry.fr/>). These data are geophysically corrected for tides, inverse barometer, tropospheric, and ionospheric signals (Dorandeu & Le Traon, 1999; Le Traon & Ogor, 1998). For the sea surface temperature, we use the SST (Foundation Temperature) Level 4 product from NAVOCEANO (GHRSSST) (<https://podaac.jpl.nasa.gov/GHRSSST>) and NOAA/NODC (AVHRR) (<https://psl.noaa.gov/data/gridded/data.noaa.oisst.v2.highres.html>), which integrates several individual sensors and provides a gridded field with error estimates. ARGO floats (<https://argo.ucsd.edu>) are also used to constrain the subsurface density structure when available over the hindcast period.

2.3. Comparison to Observed GoM Surface Drifter Velocities

To quantify the added value of the increased horizontal resolution, we compare the model velocity fields from both simulations to velocities derived from drifter trajectories over the whole GoM. From now on, we will be referring to the GoM-HYCOM 1/25° configuration as “GOM25” and to the GoM-HYCOM 1/100° configuration as “GOM100.” We use the freely available drifter data set “GulfDriftersOpen” (<https://zenodo.org/records/4421585>), details of which can be found by Lilly and Pérez-Brunius (2021). The authors gathered all publicly available drifter data in the GoM, compiled, and made them available in a single user-friendly data set that includes drifter interpolated hourly positions and velocities from 1992 to 2020.

We select velocities from drifters with a drogued, as undrogued drifters trajectories are impacted by surface winds and waves. Three independent sets of drifters types are used: CODE drifters (Davis, 1985), CARTHE drifters (Novelli et al., 2017), and SVP drifters (Lumpkin & Pazos, 2007). The CODE and CARTHE drifters have a 1 m drogued while the SVP drifters have a 15 m drogued. The tracking system of the drifters can be either Argos or GPS. Drifters before 2013 are Argos-tracked with positioning errors up to hundreds of meters (Elipot et al., 2016) and drifters after 2013 are GPS-tracked with much higher positioning accuracy (a few meters) than the Argos-tracked. Consequently, only GPS-drifters are able to resolve small-scale motions such as submesoscale eddies and waves (Lilly & Pérez-Brunius, 2021). Thus, in this study, we only use GPS-tracked same-type drifters to compare with the model outputs for the time periods when available drifter data overlap with the model outputs (2013–2020).

The three different types of drifters used in the analysis were deployed for various experiments over the time period of interest (2013–2020). The CODE drifter data used for the present analysis come from the Grand Lagrangian Deployment (GLAD; Poje et al., 2014) experiment initiated by the Consortium for Advanced Research on Transport of Hydrocarbon in the Environment (CARTHE). In total, there are ~300 CODE drifter trajectories coming from the GLAD experiment (Figure 2, left panel). Since the GLAD experiment was designed to study dispersion in the GoM (Poje et al., 2014), the drifters were deployed for a relatively short period of time and their trajectories mostly cover the eastern part of the GoM. The CARTHE drifters were deployed for the LASER (The Lagrangian Submesoscale Experiment—Haza et al., 2018; Özgökmen et al., 2018) experiment. There are ~1,300 LASER trajectories between January and March of 2016 covering a large portion of the GoM (Figure 2, middle panel). The SVP drifters were deployed as part of the GDP (Global Drifter Program; <https://www.aoml.noaa.gov/phod/gdp/index.php>) that started in September 1996. Forty-four SVP drogued drifter trajectories are available after 2013 (Figure 2, right panel). A review of all the drifter deployments mentioned here can be found in Lilly and Pérez-Brunius (2021) and references therein. We point out that drifter locations at all depths, including locations at the shelves, are used in our analyzes, which might account for some larger errors between observed and model velocities due to shelf dynamics being dependent on topographic effects. The inertial period is also not removed, which could increase the error between observed and model velocities due to errors in wind forcing (Jacobs et al., 2019).

The root mean square errors (RMSEs) between velocities from the numerical experiments and the CODE, CARTHE, and SVP drifters are shown in Figure 3. In all cases, the nearest model neighbor to the drifter's position is used to compute the RMSE. In general, GOM100 does not exhibit reduced errors (Figure 3, red lines) when compared to GOM25 (Figure 3, blue lines). In fact, in almost all cases, the error values of GOM100 and GOM25 compared to drifter velocities are either very similar or slightly higher in GOM100. This is because of the gap in the resolved scales between the observations that are assimilated in the model that primarily come from satellite altimeters and the model itself (D'Addezio et al., 2019; Jacobs et al., 2019, 2021). Higher resolution models, especially submesoscale-permitting, can produce higher errors and seemingly show less skill when compared to mesoscale-resolving ones (D'Addezio et al., 2019; Jacobs et al., 2019). The lack of RMS error improvement with an increase of the model resolution raises the question as to whether higher horizontal resolution is actually useful with respect to model skill. Jacobs et al. (2019) addressed that question by deconstructing the fields into constrained and unconstrained scales in order to filter the unconstrained small-scale variability present in their high-resolution forecast model and evaluate model skill. Constrained scales are defined as the scales at which the model is constrained by the observations assimilated. The scales that are not constrained by observations (small-scale variability) are defined as the unconstrained scales. Jacobs et al. (2019) ran several experiments of their model with different decorrelation scales to establish which decorrelation scale minimized the errors when compared to drifter trajectories from the LASER experiment. The decorrelation scale represents the spatial correlation of the initial condition model errors. When the model's initial conditions are corrected by assimilating

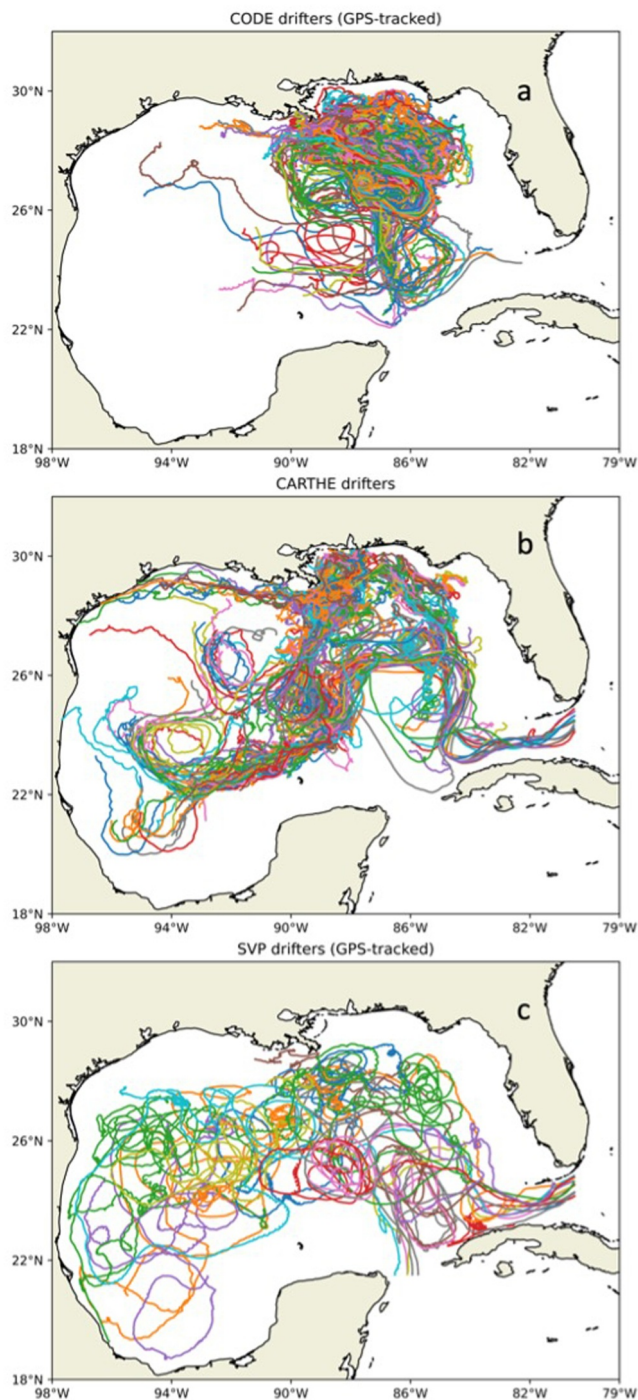


Figure 2. (a) Trajectories from CODE, (b) CARTHE, and (c) SVP drifters after 2013 for all the relevant experiments mentioned in Section 3.

observations, these observations affect their surroundings on a specific scale, which is the decorrelation scale (Jacobs et al., 2019). They then deconstructed the surface velocity field into constrained and unconstrained scales using a Gaussian convolution kernel with different length scales that were also compared against the drifter trajectories. They concluded that the lowest errors were produced using a decorrelation scale of 36 km in the model initial conditions and a Gaussian convolution kernel with an e-folding scale of 53 km in their post-processing analysis. The e-folding scale refers to the scale at which the Gaussian filter is applied to deconstruct the velocity fields. The optimal decorrelation scale and the corresponding constrained scales in GOM100 have not been directly examined. However, the use of very similar values as by Jacobs et al. (2019) is justified, since both GOM100 and the configuration used in Jacobs et al. (2019) have the same horizontal resolution.

Following their example, we use a Gaussian convolution kernel to filter out the small scales of GOM100 velocity field with a kernel standard deviation (σ) of 36.3 km, which roughly corresponds to an e-folding scale ($l = \sqrt{2}\sigma$) of 51.3 km. The main purpose is to determine how the RMSE from GOM25 compares to the RMSE from GOM100 using the same independent observations to support the hypothesis that the information extracted from the GOM100 simulation is credible. Such is possible by demonstrating that even though the total RMSE from GOM100 shows little to no improvement, it can, in fact, be reduced if the unconstrained scales are filtered out. The results are shown in Figure 3 (orange lines) for all different drifter types that were described earlier in this subsection. For the CODE and CARTHE drifters, the errors of the constrained model fields in GOM100 are reduced everywhere after filtering out the small scales when compared to the full-field errors of both GOM100 and GOM25. A similar result is obtained with the SVP drifters from the GLAD experiment, with the exception of just 1 point that corresponds to just one month where the constrained GOM100 field error is slightly larger than its GOM25 full-field counterpart. This deviation, however, is minimal, and our results therefore confirm the results put forward by Jacobs et al. (2019) regarding errors between model and observations in the constrained scales. Even though the unconstrained band is not discussed in this study, Jacobs et al. (2019, 2021) examine the importance of the unconstrained band in tandem with the constrained scales in ocean forecasting. Both studies show that the scales that are constrained by observations have deterministic predictive skill, whereas the usefulness of the unconstrained scales lies on their statistical predictability, as they contain the majority of forecast errors. Thus, they prove that there is value in progressing toward and exploring higher resolution models, as both constrained and unconstrained scales contribute to a better representation of the ocean state. Scales constrained by observations provide low error information on the large scale and mesoscale circulation and scales in the unconstrained bands yield information on small-scale variability and errors that are important as submesoscale features are directly related to their mesoscale counterparts.

2.4. Submesoscale Activity and Kinetic Energy Spectra

Figures 1a and 1b show the spatial distribution of normalized relative vorticity on 20 April 2010. The normalized relative vorticity, that is effectively the Rossby number, is defined as

$$\frac{RV}{f} = \left(\frac{\partial v}{\partial x} - \frac{\partial u}{\partial y} \right) * f^{-1}$$

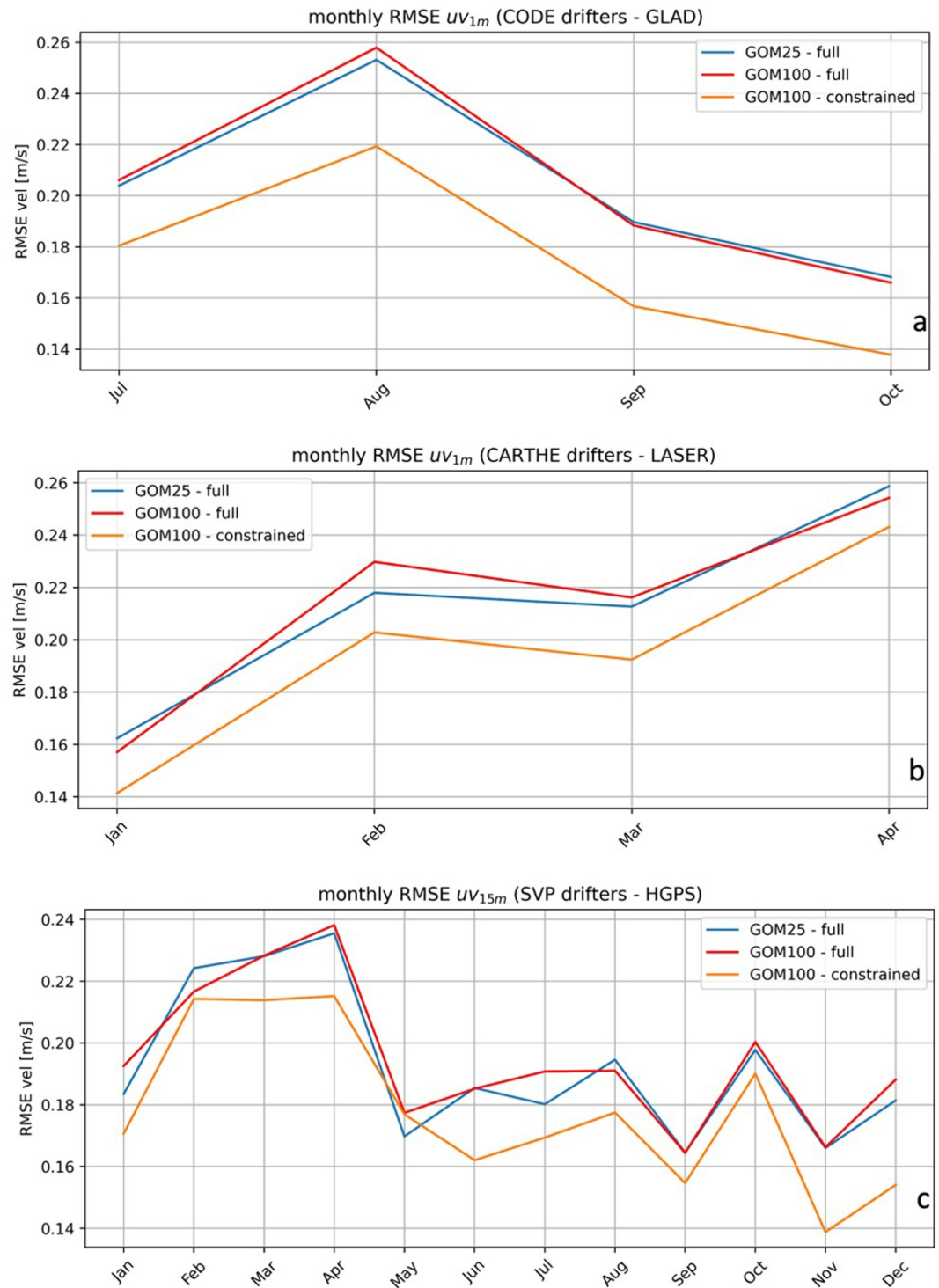


Figure 3. Full velocity RMSE between the drifter and model outputs for GOM25 (blue), GOM100 (red), and the constrained values of GOM100 (orange) for three drifter types: Shown are (a) CODE drifters from the GLAD experiment, (b) CARTHE drifters from the LASER experiment, and (c) SVP drifters (bottom panel).

where u is the zonal component of the velocity, v is the meridional component of the velocity, and f is the Coriolis parameter. An abundance of small-scale structures in the entire GoM is shown in Figure 1b, both cyclonic and anticyclonic, pointing toward a submesoscale signature that is evident in GOM100 but not in GOM25 (Figure 1a).

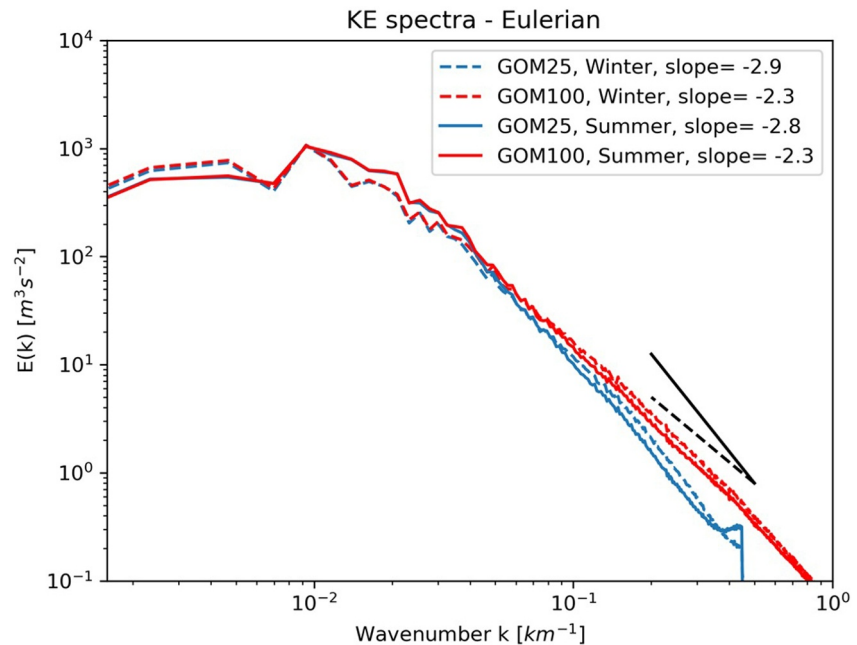


Figure 4. Kinetic energy spectra for the entire GoM region in winter (dashed blue and red) and summer (solid blue and red) of 2010 for GOM100 (red) and GOM25 (blue) experiments. The black lines represent the -3 (solid) and -2 (dashed) spectral slopes.

These structures are much smaller on the shelf regions and frontal structures that are evident in GOM25 (i.e., West Florida Shelf, Figure 1a) are thinner and accompanied by small-scale eddies in GOM100 (i.e., West Florida Shelf, Figure 1b). Small-scale structures are also evident around the Loop Current Eddy (LCE) and on the Loop Current (LC) front. A unique aspect of this comparison is that the mesoscale features are primarily constrained in both GOM25 and GOM100 via data assimilation (see Section 2.2), but that submesoscale activity is free to develop in GOM100. This allows us to state that the observed differences in advection and dispersion are primarily due to the submesoscale and not a different representation of the mesoscale. In the northeastern GoM (see black box, Figures 1a and 1b), the submesoscale activity in GOM100 is quite pronounced with both small eddies and sharp fronts. In this region, the submesoscale circulation is strongly affected by the freshwater input from the Mississippi river and is, in fact, intensified because of the frontogenesis induced by the sharp density gradients in salinity (Barkan, McWilliams, Molemaker, et al., 2017; Luo et al., 2016; Poje et al., 2014). The PDFs of RV/f are asymmetrical, exhibiting positive skewness regardless of the resolution (Figure 1c). This indicates that the region is dominated by cyclonic features in both resolutions. GOM100 PDF is characterized by longer tails toward positive RV/f values and increased skewness values compared to GOM25, a result that relates to the formation of stronger cyclonic eddies, filaments, and fronts with the increase of horizontal resolution. The longer tails that are also pronounced toward the anticyclonic values (negative RV/f) in GOM100 are similarly attributed to stronger anticyclonic features as well as a possibly stronger anticyclonic LC body when the LC northern extension is north of 26°N (southern boundary of black box in Figures 1a and 1b). The above results agree with similar findings from Zhong and Bracco (2013) and references therein as well as Schlichting et al. (2023).

The increase in model resolution also modifies the spatial distribution of kinetic energy, as there is a large increase of energy in scales smaller than 50 km in GOM100 both in winter (January, February, and March) and summer (July, August, and September) (Figure 4). The differences in kinetic energy grow larger as the scales become smaller with the spectral slopes in GOM100 (~ -2) being flatter when compared to GOM25 (~ -3) during both seasons. Slope values of -3 and steeper are representative of mesoscales and geostrophic flows (Zhong & Bracco, 2013), whereas kinetic energy spectra with slope values shallower than -3 are typical of submesoscale circulations based on horizontal model resolutions of 1 and 2 km (Barkan, McWilliams, Shchepetkin, et al., 2017; Capet et al., 2008a; Klein et al., 2008; Zhong & Bracco, 2013).

3. Lagrangian Transport and Mixing in the Northeastern GoM

The previous section described and compared the two experiments from an Eulerian point of view. In this section, we investigate the impact of resolution on Lagrangian transport and mixing in the northeastern GoM (black box, Figures 1a and 1b), one of the regions in the GoM characterized by high submesoscale activity (Figure 1b) and the location of the 2010 Deepwater Horizon oil spill. As shown in Figure 1b, the 1 km configuration (GOM100) exhibits a lot of small-scale eddies and fronts (the submesoscale soup as described by McWilliams (2016)) that are not present in GOM25 (Figure 1a).

3.1. Experimental Setup

The first step in a Lagrangian framework approach is to generate Lagrangian particle trajectories. This was achieved by using the OceanParcels Lagrangian Framework toolbox (Delandmeter & Van Sebille, 2019, <https://oceanparcels.org/>) and seeding 2-d passive particles in the northeastern GoM that are advected at the ocean surface with a 4th order Runge-Kutta advection scheme ($dt = 2h$). We performed two sets of experiments, one forward and one backward in time, each of them with 2,250,000 particles released on a $1,500 \times 1,500$ point grid (see location in Figures 1a and 1b) spaced 0.004° in the meridional direction (y) and 0.008° in the zonal direction (x). The hourly surface velocities used to advect the particles are from GOM25 and GOM100, respectively (see Section 2.1), for the entire 2010, the year of the Deepwater Horizon oil spill. Each forward-time release was repeated every 10 days and integrated forward for 3 months. The forward-time trajectories are used to calculate particle distributions and compute cumulative and total distances covered. Each backward-time release was repeated every 10 days and integrated backward for 10 days. The backward-time generated trajectories are used to identify transport barriers and attracting LCSs by calculating FTLEs.

3.2. Example of Lagrangian Trajectories

An example of particle positions for one of the forward-time releases is presented in Figure 5 for a release on 1 May 2010. The differences in trajectories between the two simulations illustrate the impact of resolving the submesoscale in GOM100. Overall, the particle distribution is more diffused around the constrained mesoscale features in GOM100 than in GOM25 with the examples of a cyclonic eddy $\sim 24^\circ N$, $87^\circ W$ where the particles are more spread out in GOM100 and features all over the Louisiana-Texas (LATEX) shelf that are also more diffused in GOM100 compared to GOM25 (Figure 5b). However, the biggest difference is found in the eastern GoM, especially over the West Florida shelf. In GOM25, the particles are distributed all over the shelf, whereas, in GOM100, they have the tendency to organize themselves along one line in the north-south direction. The cumulative distances of the particles (overall distances traveled) from the forward-time releases are quite similar in both simulations with only the medians in GOM100 being $\sim 10\%$ higher when compared to GOM25 (not shown). The small differences in cumulative distances can be attributed to higher frequency motions resulting from the submesoscale activity of GOM100.

3.3. FTLEs

FTLEs measure the separation rate of nearby fluid particles in the time interval $\tau = t - t_0$, where t_0 and t are the times for the initial and final positions of the fluid particles, respectively. FTLE is defined as

$$\sigma_i^\tau(\mathbf{x}) := |\tau|^{-1} \ln \lambda_{\max}(\Delta(\mathbf{x}; t, \tau))$$

where λ_{\max} is the maximum eigenvalue of the right Cauchy-Green deformation tensor $\Delta(\mathbf{x}; t, \tau)$, which is defined as

$$\Delta(\mathbf{x}; t, \tau) := \partial_x \phi_i^{t+\tau}(\mathbf{x})^T \partial_x \phi_i^{t+\tau}(\mathbf{x})$$

where $\phi_i^{t+\tau}(\mathbf{x})$ is the flow map defined as $\phi_i^{t+\tau} : \mathbf{x}(t) \mapsto \mathbf{x}(t + \tau)$, where $\mathbf{x}(t)$ is the position of the fluid particles at time t . The flow map $\phi_i^{t+\tau}(\mathbf{x})$ is calculated by integrating the particle trajectories from $t = t_0$ to $t = t + \tau$. FTLEs represent the maximal rate of mixing (stretching/folding) about the particle trajectory and can be calculated either in forward ($\tau > 0$) or in backward time ($\tau < 0$). Ridges of FTLE's are indicators of LCSs (Haller, 2002; Shadden et al., 2005). Ridges of forward-time FTLEs identify repelling LCSs, whereas ridges of

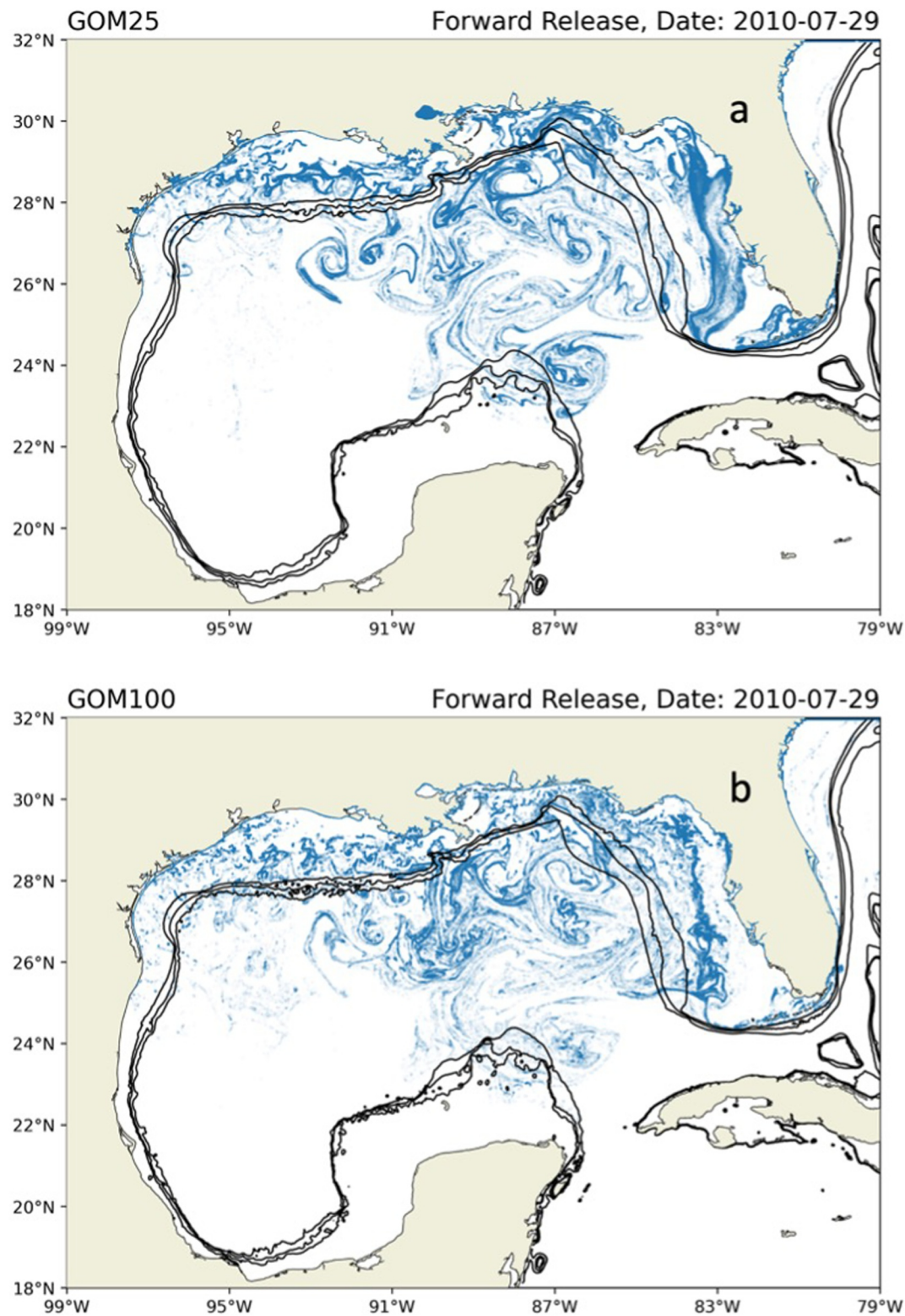


Figure 5. Particle positions at the end of a 90-day forward-time release in the northeast GoM (black box in Figures 1a and 1b) and initiated on 1 May 2010—(a) GOM25 and (b) GOM100. The solid black lines represent the 100, 200, and 500 m-isobaths.

backward-time FTLEs indicate attracting LCSs (for a schematic illustration, see Farazmand & Haller, 2013). However, both attracting and repelling LCSs can be identified from a single chunk of data (without selecting from forward- or backward-time calculations) by calculating the maximum and minimum eigenvectors of the Cauchy-Green tensor (Farazmand & Haller, 2013). Repelling LCSs are a metric for maximal local stretching, whereas attracting LCSs are linked to regions where oceanic passive tracers accumulate (Beron-Vera, 2010; Beron-Vera et al., 2008; Farazmand & Haller, 2013; Olascoaga & Haller, 2012). LCSs are surfaces of local FTLE maxima or curvature ridges of the FTLE field (Shadden et al., 2005). As shown by Shadden et al. (2005), to extract the LCSs, we first need to define the curvature of the FTLE field, given by the Hessian matrix Σ . Hessian matrix is a square matrix of second order partial derivatives of a scalar function, such as the FTLE and determines points of local maxima and minima. Σ is defined as

$$\Sigma := \frac{d^2 \sigma_t^{+\tau}(\mathbf{x})}{d\mathbf{x}^2}$$

where σ is the FTLE field. To, then, identify a curvature ridge (second-derivative ridge), the smallest eigenvalue of Σ , λ_n and its eigenvector \mathbf{n} need to satisfy the following conditions:

$$\lambda_n < 0 \text{ and } \nabla \sigma \cdot \mathbf{n} = \mathbf{0} \text{ (vectors } \nabla \sigma \text{ and } \mathbf{n} \text{ must be parallel)}$$

When these conditions are met, they define a curve that moves in time, that is, the LCS. Since we are interested in identifying regions of passive particle convergence, we will be focusing on backward-time FTLE calculations with $\tau = -10$ days and attracting LCSs. The attracting LCSs stem from advective mixing and characterize regions of accumulation (Allshouse & Peacock, 2015; Beron-Vera, 2010; Haller, 2001a; Perez et al., 2021). The chosen time interval of 10 days allows us to capture short-lived, finer-scale patterns (Sinha et al., 2019).

The FTLE calculations are conducted with the purpose of identifying possible changes in transport barriers and mixing in the northeastern GoM as the model resolution increases from 4 to 1 km. FTLEs provide a description of how mixing and transport are organized around the transport barriers that are marked by the FTLE ridges (Haller & Yuan, 2000; Shadden et al., 2005). Shadden et al. (2005) also showed that the flux of FTLEs along the Lagrangian ridges is minimal, proving that they are almost material lines. The notion of material lines, extensively discussed in the theory of dynamical systems, denotes a flow barrier that distinguishes fluids with different properties. Finally, it is important to note that an FTLE field is of a diagnostic nature in terms of mixing and does not give information on the features of the velocity field, such as reference frame dependence/independence, that was used to generate the particle trajectories (Haller, 2001b).

3.4. Chaotic Advection Versus Turbulent Mixing

To further investigate the differences in Lagrangian transport between the two data-assimilative numerical simulations, we performed backward-time particle experiments conducted every 10 days for 1 year starting on 1 January 2010. The simulated trajectories are used to calculate FTLEs and the associated LCSs, snapshots of which are shown in Figure 6. The snapshots provide an example of a winter distribution (Figures 6a–6d) and of a summer one (Figures 6e–6h), which are representative of the Lagrangian picture throughout the year as will be discussed later in this section.

In the winter month example, the FTLE fields and respective LCSs in GOM25 (Figures 6a and 6b) reveal a plethora of eddy structures that are present in the entire region with smaller scale eddies consistently appearing in the shelf regions. A similar picture is present in GOM100 (Figures 6c and 6d) but more convoluted than in GOM25. Thus, an abundance of LCSs is also prevalent in GOM100 (Figure 6d) but of smaller scales and covering a much larger area when compared to GOM25 (Figure 6b). Overall, the smaller structures that emerge in GOM100 follow the patterns of GOM25, indicating that the submesoscale in GOM100 is allowed to evolve within the larger mesoscale picture, as depicted in GOM25. In the summer month example, in both GOM25 and GOM100, the mesoscale fields are more elongated and there are more frontal structures (Figures 6e–6h). This is consistent with Choi et al. (2017) and Bracco et al. (2019) who documented the appearance of more fronts in summer and more eddies in winter in the northern GoM, even though fronts and eddies are always present regardless of the season. Finally, the FTLE fields are smoother in summer than in winter, in both GOM25 and GOM100, possibly because of the relaxed wind forcing during the summer months.

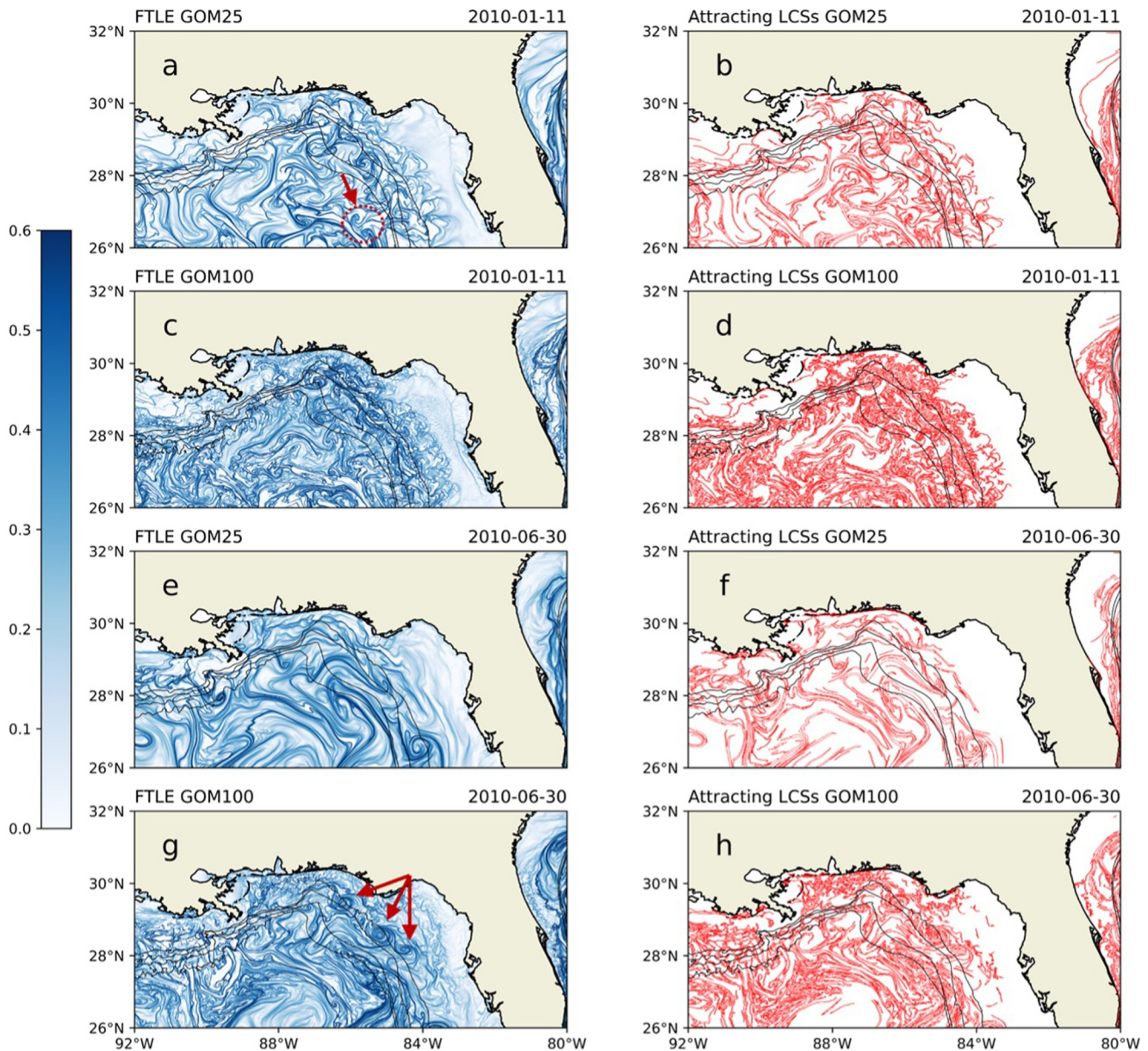


Figure 6. Backward-time normalized FTLE fields and attracting LCSs for two 10-day time intervals ending on 2010-01-11 in (a)–(d) and 2010-06-30 in (e)–(h). Panels (a), (c), (e), and (g) show the normalized FTLE fields, and panels (b), (d), (f), and (h) show the attracting LCSs extracted from the respective FTLE fields. The solid black lines represent the 100, 200, 500, and 1,000 m-isobaths, respectively. The red arrows indicate examples of a mushroom-like feature in (a) and spiral-like one in (g).

Generally, the seasonality in scales up to 10 km can be attributed to the submesoscale field that generally intensifies in the winter and weakens in the summer (Bracco et al., 2019). The mixed layer instabilities behind the generation of submesoscale features grow in the winter when the mixed layer is deep and weaken during the summer when the mixed layer is shallower (Bracco et al., 2019; Callies et al., 2015; Chassignet & Xu, 2017; Thompson et al., 2016). However, the seasonality in the submesoscale features does not always follow this pattern depending on the region of the northern GoM. For example, the LATEX shelf exhibits baroclinic instabilities in the summer because of the Mississippi-Atchafalaya plume (Hetland, 2017; Qu et al., 2022). According to these studies, when river plumes are present, instabilities are suppressed through strong mixing during winter when winds are intensified. In contrast, the weakening of winds in the summer promotes plume instabilities that generate a rich eddy field. Such happens in the case of the Mississippi-Atchafalaya plume that goes through instabilities in the summer when the winds are weak. For scales larger than 10 km, mixed layer instabilities do not

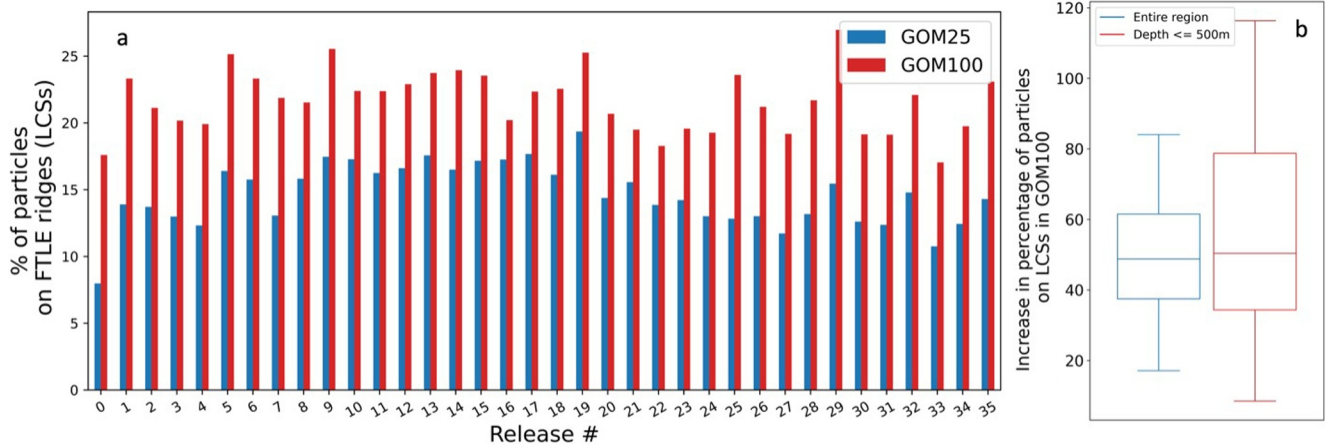


Figure 7. (a) Percentage of particles that ended up on FTLE ridges for all backward-time particle releases in 2010 for GOM25 (blue) and GOM100 (red) and (b) boxplots of increase of particles that end up on FTLE ridges in GOM100 compared to GOM25 in the entire region (blue) and shelf regions with depths ≤ 500 m (red).

exhibit a strong seasonal cycle (Callies et al., 2015). Evidence of eddies and fronts smaller than 10 km is shown in the FTLE fields of both GOM25 and GOM100, as the computation of FTLE is not bound by the velocity field resolution (Beron-Vera, 2010) that only allows for structures greater than 10 km based on the 1 km grid spacing of GOM100.

Similarly to the winter case, in GOM100 (Figures 6g and 6h), ridges of FTLEs in the summer lie within the larger mesoscale picture of GOM25 (Figures 6e and 6f). In both experiments and regardless of the season, the increased amount and intricacy of LCSs, as well as the higher FTLE values in GOM100, further indicate that the mixing produced by GOM100 velocity fields is more vigorous. Both FTLE fields and LCSs show spiral-like and mushroom-like patterns, which indicate eddies (either cyclonic or anticyclonic) and eddy dipoles, respectively (Beron-Vera et al., 2008). An example of a mushroom-like pattern is shown in GOM25 on the West Florida Shelf $\sim 27^\circ\text{N}$ and 84°W (see arrow and circle in Figure 6a). An example of spiral-like patterns is indicated in GOM100 where three consecutive spiral-like patterns are present along the West Florida Shelf between 27°N and 29°N (see arrows in Figure 6g). Overall, more intricate LCSs are produced in GOM100 and higher FTLE values (bolder colors) indicate transport barriers that are more intense in the submesoscale-permitting simulation.

The comparison of FTLE fields between the two simulations also provides some information as to whether chaotic advection dominates over turbulent mixing or vice versa. Chaotic mixing or advection is related to mixing by organized invariant manifolds or Lagrangian coherent structures (Beron-Vera, 2010; Beron-Vera & Olascoaga, 2009; Brown & Smith, 1991; Budyansky et al., 2007; Koshel' and Prants, 2006; Pierrehumbert, 1991). Turbulent mixing is related to incoherent and irregular flow, whereas chaotic advection refers to quasi-regular flow. In both cases (winter and summer), the FTLE fields clearly show similarities with respect to the larger mesoscale picture, since in the higher resolution GOM100 simulation, smaller scale coherent structures emerge within the larger mesoscale picture characterized by GOM25. Thus, the large-scale transport barriers remain almost the same with the increase of resolution. In this set of experiments, we therefore find that Lagrangian mixing manifests in the form of LCSs (Figures 6b, 6d, 6f, and 6h) regardless of the resolution. Thus, the two-dimensional surface flow is dominated by chaotic advection. If the flow was dominated by turbulent mixing, then the Lagrangian calculations would not display any similarities in transport barriers or large-scale LCSs, since turbulent mixing is inherent to irregular and incoherent flow. However, the convoluted higher-detailed GOM100, with the emergence of small-scale noise-like filaments not present in GOM25 (Figures 6d and 6h), suggest that the component of turbulent mixing is more prevalent in GOM100 than in GOM25. Further information on the prevalence of chaotic advection over turbulent mixing is provided later in this section.

There is a larger number of particles accumulating on FTLE ridges or LCSs in GOM100 than in GOM25 (Figure 7a), a result associated with stronger Lagrangian transport and mixing in GOM100. More specifically, in GOM100, the percentage of LCS particles (red bars, Figure 7a) is persistently higher than in GOM25 (blue bars, Figure 7a), a result that is in agreement with the discussion of Figure 6. This further supports the hypothesis that the northeastern GoM is more energetic in the high-resolution simulation even in a region away from the LC core.

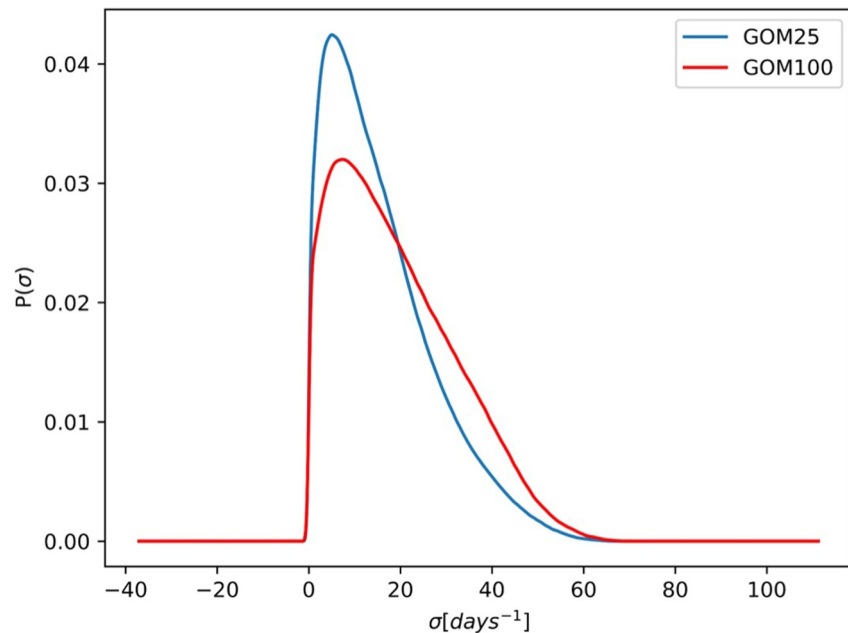


Figure 8. PDFs of backward-time FTLEs for all 10-day particle releases in 2010 for GOM25 (blue) and GOM100 (red). The skewness values are 0.97 for GOM25 PDF and 0.65 for GOM100.

Overall, there is a median of $\sim 50\%$ increase in LCS particles in GOM100 over GOM25 in both the entire northeastern GoM and shelf regions with depths ≤ 500 m (Figure 7b). However, the range of the increase is higher on the shelves when compared to the entire region. Consequently, higher FTLE differences between GOM25 and GOM100 are exhibited on the shelves compared to the entire region assessed, indicating that shelf dynamics become more energetic compared to the entire region with the increase of resolution. Such a result underlies the importance of shelf dynamics on mixing in the GoM especially in the West Florida Shelf (Beron-Vera & Olascoaga, 2009; Choi et al., 2017; Olascoaga, 2010; Olascoaga et al., 2006; Yang et al., 1999) and on applications such as oil spill simulations and biogeochemical modeling.

The PDFs of FTLEs for both GOM25 and GOM100 are positively skewed with long tails toward the shorter timescales with GOM100 exhibiting a longer tail (Figure 8). The longer tail indicates the presence of intense and short-lived events, such as the presence of submesoscale eddies that form and dissipate over a short time period. The asymmetry of the PDFs further implies that chaotic advection dominates turbulent mixing, as discussed earlier. The PDFs would be symmetrical if the situation was reversed, if turbulent mixing was dominant. The PDF of the GOM100 FTLE fields is slightly less skewed than the GOM25 case, suggesting that the influence of turbulent mixing is slightly larger in GOM100. The heterogeneity of the particle mixing at the surface therefore supports the hypothesis that there is value-added in the increased resolution. The lack of multiple extrema in the PDFs suggests that persistent features are not present and most of the features are short-lived or transient (Beron-Vera & Olascoaga, 2009). Similar results were produced by Waugh and Abraham (2008) for the global ocean, Beron-Vera (2010) in the Agulhas and ACC regions using altimetry-derived currents, and Beron-Vera and Olascoaga (2009) in the West Florida Shelf using HYCOM outputs.

4. Oil Particle Simulations

Among the variety of applications that could benefit from this study are oil spills with respect to differences in the modeling of oil particle dispersion based on the velocity field horizontal and/or vertical resolution. To illustrate this, two experiments were conducted to provide an initial estimate of differences in oil particle spread as a function of the numerical model's horizontal grid spacing. We use Openoil (<https://opendrifty.github.io/autoapi/opendrifty/models/openoil/index.html>), a 3D oil drift module for oil particle advection and oil spill simulation distributed by Opendrifty (<https://opendrifty.github.io/index.html>). Opendrifty is a Lagrangian framework package similar to OceanParcels that was used for the passive particle advection described in Section 3.1. OceanParcels could not be used for oil particle advection, as it does not offer an equivalent oil drift module like Openoil.

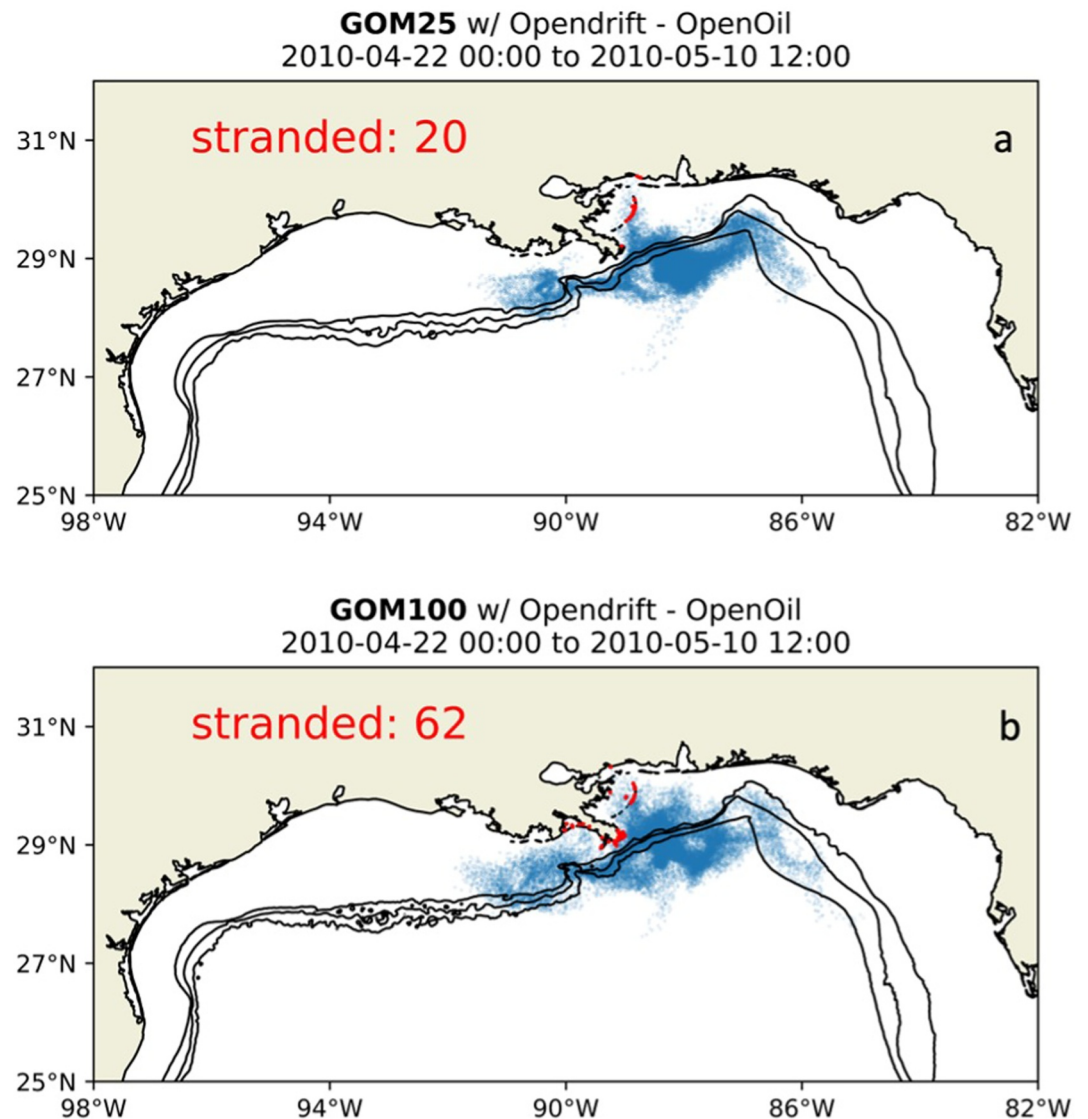


Figure 9. 12-hourly oil particle positions from 22 April 2010 to 10 May 2010 (blue colors). The black dot represents the initial positions of 1,000 oil particles in a 5 km radius at the Deepwater Horizon location (28.7°N, 88.4°W) using the velocity fields from (a) GOM25 and (b) GOM100 (bottom). The red dots represent oil particles that are stranded on the shore. The solid black lines represent the 100, 200, and 500 m-isobaths.

The two examples, shown in Figure 9, were initialized at the location of the Deepwater Horizon spill (28.7°N, 88.4°W) and conducted for 1 month using surface velocity fields from GOM25 and GOM100 in April–May 2010. The oil weathering calculations use the NOAA-ERR_ERD OilLibrary package. This package uses the NOAA database for oil droplet densities based on the oil types that are selected for the experiments and calculates oil evaporation and emulsification in the simulations. Starting on 22 April 2010, the day that oil reached the ocean surface for the first time, 1,000 oil particles were released at the surface in a 5 km radius and tracked until the end of May 2010. The purpose of this preliminary experiment is to showcase that GOM100 performs better than GOM25 in the initial stages of the oil spill simulation based on the timeline of the oil spill accident in 2010. Bracco et al. (2019) noted that forecast models at the time (of maximum 5 km horizontal resolution) failed to correctly forecast the arrival of the oil at the coast of Louisiana, as they predicted a later arrival. News articles started reporting the arrival of oil at the uninhabited barrier islands of Louisiana late on 29 April 2010 (“Flashback: BP oil spill, 2024,” “Oil slick reaches US coast earlier than expected, 2024,” “Wildlife threatened by oil, 2024”) and that oil had reached the mainland of Louisiana, at Port Eads, located at the Mississippi river mouth,

on 10 May 2010 (“Patches of Oil Wash Ashore in Louisiana, 2024”). Based on the above timeline of the oil spill in 2010, GOM100 is more realistic than GOM25, as oil particles reach the shore faster than in GOM25. Initially, the first stranded particles appear on April 29 in GOM100 (see animation of oil particle evolution in Supporting Information S1), however, not on the barrier islands but on the mainland of Louisiana. By 10 May 2010 (Figure 9b), 62 particles have reached the mainland of Louisiana in GOM100. In contrast, almost no particles are captured either at the river mouth or other regions of the mainland in GOM25 (Figure 9a). Such shows that even preliminary oil particle experiments track the realistic timeline of the tragic accident better in GOM100 than in GOM25.

Other general differences in the oil particle positions between the two resolutions are clearly visible early on (Figure 9). By 10 May 2010 more oil particles have spread over waters shallower than 100 m in GOM100 compared to GOM25. By the end of the simulation (22 May 2010—see animation in Supporting Information S1), approximately 30% more GOM100 oil particles end up stranded on land when compared to the GOM25 particles. This still remains to be compared against the realistic spread of the Deepwater Horizon oil spill, but the differences illustrate the impact of small-scale ocean features on oil dispersion. Finally, we note that for a realistic simulation of the Deepwater Horizon oil spill, one would need to include more features such as a plume model, 3D advection, etc. In addition, ensemble simulations of GOM100 would be useful to address velocity uncertainties aiming to ultimately improve the velocity representation and subsequent oil particle simulations. In the case of an oil spill, the calculations of FTLE fields in ocean forecasts would provide guidance to first responders on where one may be able to track accumulation of oil, as oil particles tend to organize themselves along material lines.

5. Summary and Conclusions

In this paper, the importance of model horizontal resolution in mixing and dispersion was evaluated by comparing two data-assimilative, high-resolution simulations ($1/25^\circ$ —4 km and $1/100^\circ$ —1 km), the latter being submesoscale-permitting. By employing both Eulerian and Lagrangian metrics, upper-ocean differences in the context of mixing between the mesoscale- and submesoscale-permitting simulations are examined by conducting Lagrangian experiments to track the generation of Lagrangian coherent structures (LCSs) and their associated transport barriers.

The added value of the increased resolution was first explored by comparing surface velocity fields from both simulations with independent drifter observations. Drifter trajectories from various experiments between 2013 and 2020 were used, separated by drifter type: CARTHE, SVP, and CODE drifters. In all three comparisons, GOM100 yielded reduced RMSEs after filtering out the unconstrained scales in the model (D’Addezio et al., 2019; Jacobs et al., 2019, 2021), supporting the hypothesis that there is value added in resolving higher resolutions. There is higher kinetic energy in the larger wavenumbers in GOM100 and the slopes of the kinetic energy spectra are shallower (~ -2) than in GOM25, a consequence of the submesoscale activity in GOM100 with small-scale vortices, meanders, and filaments that are not present/resolved in GOM25.

To investigate differences in mixing and dispersion between the two simulations, we calculated backward-time finite-time Lyapunov exponents (FTLEs) and their associated LCSs. FTLEs measure the finite-time separation rate of nearby fluid particles and the average rate of stretching about a particle trajectory. Curvature ridges of backward in time FTLEs are indicators of attracting LCSs that act as accumulation and convergence regions, which drive the fate of dispersants in the ocean. The boundaries of LCSs mark transport barriers that separate fluids with different advection properties that are approximately immiscible during the time interval of FTLE calculation. To calculate FTLEs, we first conducted 2-D particle experiments every 10 days starting on 1 January 2010 until the end of 2010 in the northeastern GoM, a region characterized by high submesoscale activity. GOM100 exhibited higher separation rates with more intricate LCSs, demonstrating that mixing is more vigorous in the submesoscale-permitting simulation. The asymmetry of the PDFs of FTLEs in both experiments further suggests that chaotic advection dominates over turbulent mixing at the surface, although lower heterogeneity was detected in GOM100. The positive skewness of the PDFs of FTLEs in both simulations thus indicates that chaotic advection is prevalent, as opposed to symmetrical PDFs that would imply mixing is mainly turbulent. The generation of more complex LCSs in the submesoscale-permitting simulation related to coherent eddies and fronts that are not resolved in the mesoscale-resolving one highlights the significance of the horizontal resolution increase in numerical modeling.

Finally, the impact of resolution was explored by comparing the spread of oil particle trajectories in both simulations and initialized at the location of the 2010 Deepwater Horizon oil spill. The trajectories are clearly impacted by the horizontal resolution increase with more oil particles reaching the coastlines of the northern GoM, if advected using surface velocities from the submesoscale-permitting simulation. Further investigation of these patterns, alongside available observational data will provide more insight on the importance of resolving finer scales for monitoring such events. This result further underlies that Lagrangian flow applications, such as predicting the fate of dispersants, can benefit from progress in numerical modeling.

It is worth noting that future work is needed to assess mixing and dispersion at depth; identifying differences in the structure of the complex GoM dynamics at various depths would yield a more complete analysis of the impact of horizontal resolution below the direct effect of data assimilation in the system. Also, quantifying the fully three-dimensional dispersion and turbulent mixing from Eulerian metrics would provide additional insights into ocean transport and mixing. As shown in the study by Schlichting et al. (2023) in the Texas-Louisiana continental shelf, higher submesoscale-resolving model horizontal resolution highly influences mixing processes by decreasing numerical mixing and increasing physical mixing. Finally, 3-D oil particle simulations, alongside FTLE calculations at the appropriate timescales for such applications, would be beneficial to provide additional results on the value of the added resolution on the representation of the GoM dynamics from a Lagrangian perspective.

Data Availability Statement

The HYCOM-TSIS simulations used for this study are available on <https://www.hycom.org/data/gomb0pt04/gom-reanalysis> (GOM25) and <https://www.hycom.org/data/gomb0pt01/gom-reanalysis> (GOM100). Colormaps of Figures 1a and 1b were made Matplotlib's cmocean package (<https://matplotlib.org/cmocean/>—Thyng et al., 2016).

Acknowledgments

We acknowledge support from the Bureau of Ocean Energy Management under award number M20AC10020-40 and the Gulf Research Program of the National Academies of Sciences, Engineering, and Medicine under award number 2000013149. The content is solely the responsibility of the authors and does not necessarily represent the official views of the Bureau of Ocean Energy Management, the Gulf Research Program, or the National Academies of Sciences, Engineering, and Medicine.

References

- Allshouse, M. R., & Peacock, T. (2015). Refining finite-time Lyapunov exponent ridges and the challenges of classifying them. *Chaos: An Interdisciplinary Journal of Nonlinear Science*, 25(8), 087410. <https://doi.org/10.1063/1.4928210>
- Aref, H. (1984). Stirring by chaotic advection. *Journal of Fluid Mechanics*, 143, 1–21. <https://doi.org/10.1017/S0022112084001233>
- Aref, H., Blake, J. R., Budišić, M., Cardoso, S. S. S., Cartwright, J. H. E., Clercx, H. J. H., et al. (2017). Frontiers of chaotic advection. *Reviews of Modern Physics*, 89(2), 025007. <https://doi.org/10.1103/RevModPhys.89.025007>
- Barkan, R., McWilliams, J. C., Molemaker, M. J., Choi, J., Srinivasan, K., Shchepetkin, A. F., & Bracco, A. (2017). Submesoscale dynamics in the northern Gulf of Mexico. Part II: Temperature–salinity relations and cross-shelf transport processes. *Journal of Physical Oceanography*, 47(9), 2347–2360. <https://doi.org/10.1175/JPO-D-17-0040.1>
- Barkan, R., McWilliams, J. C., Shchepetkin, A. F., Molemaker, M. J., Renault, L., Bracco, A., & Choi, J. (2017). Submesoscale dynamics in the northern Gulf of Mexico. Part I: Regional and seasonal characterization and the role of river outflow. *Journal of Physical Oceanography*, 47(9), 2325–2346. <https://doi.org/10.1175/JPO-D-17-0035.1>
- Beron-Vera, F. J. (2010). Mixing by low- and high-resolution surface geostrophic currents. *Journal of Geophysical Research*, 115(C10), 2009JC006006. <https://doi.org/10.1029/2009JC006006>
- Beron-Vera, F. J., & LaCasce, J. H. (2016). Statistics of simulated and observed pair separations in the Gulf of Mexico. *Journal of Physical Oceanography*, 46(7), 2183–2199. <https://doi.org/10.1175/JPO-D-15-0127.1>
- Beron-Vera, F. J., & Olascoaga, M. J. (2009). An assessment of the importance of chaotic stirring and turbulent mixing on the West Florida Shelf. *Journal of Physical Oceanography*, 39(7), 1743–1755. <https://doi.org/10.1175/2009JPO4046.1>
- Beron-Vera, F. J., Olascoaga, M. J., & Goni, G. J. (2008). Oceanic mesoscale eddies as revealed by Lagrangian coherent structures: Oceanic mesoscale eddies as revealed by LCSS. *Geophysical Research Letters*, 35(12), L12603. <https://doi.org/10.1029/2008GL033957>
- Bleck, R. (2002). An oceanic general circulation model framed in hybrid isopycnic–Cartesian coordinates. *Ocean Modelling*, 4(1), 55–88. [https://doi.org/10.1016/S1463-5003\(01\)00012-9](https://doi.org/10.1016/S1463-5003(01)00012-9)
- Bracco, A., Liu, G., & Sun, D. (2019). Mesoscale-submesoscale interactions in the Gulf of Mexico: From oil dispersion to climate. *Chaos, Solitons and Fractals*, 119, 63–72. <https://doi.org/10.1016/j.chaos.2018.12.012>
- Brown, M. G., & Smith, K. B. (1991). Ocean stirring and chaotic low-order dynamics. *Physics of Fluids A: Fluid Dynamics*, 3(5), 1186–1192. <https://doi.org/10.1063/1.858047>
- Budyansky, M. V., Uleysky, M. Y., & Prants, S. V. (2007). Lagrangian coherent structures, transport and chaotic mixing in simple kinematic ocean models. *Communications in Nonlinear Science and Numerical Simulation*, 12(1), 31–44. <https://doi.org/10.1016/j.cnsns.2006.01.008>
- Callies, J., Ferrari, R., Klymak, J. M., & Gula, J. (2015). Seasonality in submesoscale turbulence. *Nature Communications*, 6(1), 6862. <https://doi.org/10.1038/ncomms7862>
- Capet, X., McWilliams, J. C., Molemaker, M. J., & Shchepetkin, A. F. (2008a). Mesoscale to submesoscale transition in the California current system. Part I: Flow structure, eddy flux, and observational tests. *Journal of Physical Oceanography*, 38(1), 29–43. <https://doi.org/10.1175/2007JPO3671.1>
- Capet, X., McWilliams, J. C., Molemaker, M. J., & Shchepetkin, A. F. (2008b). Mesoscale to submesoscale transition in the California current system. Part III: Energy balance and flux. *Journal of Physical Oceanography*, 38(10), 2256–2269. <https://doi.org/10.1175/2008JPO3810.1>
- Capet, X., McWilliams, J. C., Molemaker, M. J., & Shchepetkin, A. F. (2008c). Mesoscale to submesoscale transition in the California current system. Part II: Frontal processes. *Journal of Physical Oceanography*, 38(1), 44–64. <https://doi.org/10.1175/2007JPO3672.1>

- Chassignet, E. P., Smith, L. T., Halliwell, G. R., & Bleck, R. (2003). North Atlantic simulations with the hybrid coordinate ocean model (HYCOM): Impact of the vertical coordinate choice, reference pressure, and thermobaricity. *Journal of Physical Oceanography*, 33(12), 2504–2526. [https://doi.org/10.1175/1520-0485\(2003\)033<2504:NASWTH>2.0.CO;2](https://doi.org/10.1175/1520-0485(2003)033<2504:NASWTH>2.0.CO;2)
- Chassignet, E. P., & Xu, X. (2017). Impact of horizontal resolution (1/12° to 1/50°) on Gulf Stream separation, penetration, and variability. *Journal of Physical Oceanography*, 47(8), 1999–2021. <https://doi.org/10.1175/JPO-D-17-0031.1>
- Choi, J., Bracco, A., Barkan, R., Shchepetkin, A. F., McWilliams, J. C., & Molemaker, J. M. (2017). Submesoscale dynamics in the northern Gulf of Mexico. Part III: Lagrangian implications. *Journal of Physical Oceanography*, 47(9), 2361–2376. <https://doi.org/10.1175/JPO-D-17-0036.1>
- Cooper, M., & Haines, K. (1996). Altimetric assimilation with water property conservation. *Journal of Geophysical Research*, 101(C1), 1059–1077. <https://doi.org/10.1029/95JC02902>
- D'Addezio, J. M., Smith, S., Jacobs, G. A., Helber, R. W., Rowley, C., Souopgui, I., & Carrier, M. J. (2019). Quantifying wavelengths constrained by simulated SWOT observations in a submesoscale resolving ocean analysis/forecasting system. *Ocean Modelling*, 135, 40–55. <https://doi.org/10.1016/j.ocemod.2019.02.001>
- D'Asaro, E., Lee, C., Rainville, L., Harcourt, R., & Thomas, L. (2011). Enhanced turbulence and energy dissipation at ocean fronts. *Science*, 332(6027), 318–322. <https://doi.org/10.1126/science.1201515>
- Davis, R. E. (1985). Drifter observations of coastal surface currents during CODE: The method and descriptive view. *Journal of Geophysical Research*, 90(C3), 4741–4755. <https://doi.org/10.1029/JC090iC03p04741>
- Delandmeter, P., & Van Sebille, E. (2019). The parcels v2.0 Lagrangian framework: New field interpolation schemes. *Geoscientific Model Development*, 12(8), 3571–3584. <https://doi.org/10.5194/gmd-12-3571-2019>
- Dorandeu, J., & Le Traon, P. Y. (1999). Effects of global mean atmospheric pressure variations on mean sea level changes from TOPEX/Poseidon. *Journal of Atmospheric and Oceanic Technology*, 16(9), 1279–1283. [https://doi.org/10.1175/1520-0426\(1999\)016<1279:EOGMAP>2.0.CO;2](https://doi.org/10.1175/1520-0426(1999)016<1279:EOGMAP>2.0.CO;2)
- Egbert, G. D., & Erofeeva, S. Y. (2002). Efficient inverse modeling of barotropic ocean tides. *Journal of Atmospheric and Oceanic Technology*, 19(2), 183–204. [https://doi.org/10.1175/1520-0426\(2002\)019<0183:EIMOBO>2.0.CO;2](https://doi.org/10.1175/1520-0426(2002)019<0183:EIMOBO>2.0.CO;2)
- Eliot, S., Lumpkin, R., Perez, R. C., Lilly, J. M., Early, J. J., & Sykulski, A. M. (2016). A global surface drifter data set at hourly resolution. *Journal of Geophysical Research: Oceans*, 121(5), 2937–2966. <https://doi.org/10.1002/2016JC011716>
- Evensen, G. (2003). The ensemble Kalman filter: Theoretical formulation and practical implementation. *Ocean Dynamics*, 53(4), 343–367. <https://doi.org/10.1007/s10236-003-0036-9>
- Farazmand, M., & Haller, G. (2013). Attracting and repelling Lagrangian coherent structures from a single computation. *Chaos: An Interdisciplinary Journal of Nonlinear Science*, 23(2), 023101. <https://doi.org/10.1063/1.4800210>
- Flashback: BP oil spill. (2024). *Flashback: BP oil spill*. Reuters. Retrieved from <https://www.reuters.com/news/picture/flashback-bp-oil-spill-idJPRTR2LEJ6/>
- Haller, G. (2001a). Distinguished material surfaces and coherent structures in three-dimensional fluid flows. *Physica D: Nonlinear Phenomena*, 149(4), 248–277. [https://doi.org/10.1016/S0167-2789\(00\)00199-8](https://doi.org/10.1016/S0167-2789(00)00199-8)
- Haller, G. (2001b). Lagrangian structures and the rate of strain in a partition of two-dimensional turbulence. *Physics of Fluids*, 13(11), 3365–3385. <https://doi.org/10.1063/1.1403336>
- Haller, G. (2002). Lagrangian coherent structures from approximate velocity data. *Physics of Fluids*, 14(6), 1851–1861. <https://doi.org/10.1063/1.1477449>
- Haller, G., & Yuan, G. (2000). Lagrangian coherent structures and mixing in two-dimensional turbulence. *Physica D: Nonlinear Phenomena*, 147(3–4), 352–370. [https://doi.org/10.1016/S0167-2789\(00\)00142-1](https://doi.org/10.1016/S0167-2789(00)00142-1)
- Haza, A. C., D'Asaro, E., Chang, H., Chen, S., Curcic, M., Guigand, C., et al. (2018). Drogue-loss detection for surface drifters during the Lagrangian submesoscale experiment (LASER). *Journal of Atmospheric and Oceanic Technology*, 35(4), 705–725. <https://doi.org/10.1175/JTECH-D-17-0143.1>
- Hetland, R. D. (2017). Suppression of baroclinic instabilities in Buoyancy-driven flow over sloping bathymetry. *Journal of Physical Oceanography*, 47(1), 49–68. <https://doi.org/10.1175/JPO-D-15-0240.1>
- Jacobs, G., D'Addezio, J. M., Ngodock, H., & Souopgui, I. (2021). Observation and model resolution implications to ocean prediction. *Ocean Modelling*, 159, 101760. <https://doi.org/10.1016/j.ocemod.2021.101760>
- Jacobs, G. A., D'Addezio, J. M., Bartels, B., & Spence, P. L. (2019). Constrained scales in ocean forecasting. *Advances in Space Research*, 68(2), 746–761. <https://doi.org/10.1016/j.asr.2019.09.018>
- Klein, P., Hua, B. L., Lapeyre, G., Capet, X., Le Gentil, S., & Sasaki, H. (2008). Upper ocean turbulence from high-resolution 3D simulations. *Journal of Physical Oceanography*, 38(8), 1748–1763. <https://doi.org/10.1175/2007JPO3773.1>
- Koshel, K. V., & Prants, S. V. (2006). Chaotic advection in the ocean. *Physics-Uspekhi*, 49(11), 1151–1178. <https://doi.org/10.1070/PU2006v049n11ABEH006066>
- Large, W. G., McWilliams, J. C., & Doney, S. C. (1994). Oceanic vertical mixing: A review and a model with a nonlocal boundary layer parameterization. *Reviews of Geophysics*, 32(4), 363–403. <https://doi.org/10.1029/94RG01872>
- Le Traon, P.-Y., & Ogor, F. (1998). ERS-1/2 orbit improvement using TOPEX/POSEIDON: The 2 cm challenge. *Journal of Geophysical Research*, 103(C4), 8045–8057. <https://doi.org/10.1029/97JC01917>
- Lilly, J. M., & Pérez-Brunius, P. (2021). A gridded surface current product for the Gulf of Mexico from consolidated drifter measurements. *Earth System Science Data*, 13(2), 645–669. <https://doi.org/10.5194/essd-13-645-2021>
- Liu, G., Bracco, A., & Passow, U. (2018). The influence of mesoscale and submesoscale circulation on sinking particles in the northern Gulf of Mexico. *Elementa: Science of the Anthropocene*, 6, 36. <https://doi.org/10.1525/elementa.292>
- Liu, G., Bracco, A., & Sitar, A. (2021). Submesoscale mixing across the mixed layer in the Gulf of Mexico. *Frontiers in Marine Science*, 8, 615066. <https://doi.org/10.3389/fmars.2021.615066>
- Liu, Y., Weisberg, R. H., Hu, C., & Zheng, L. (2011). Tracking the deepwater horizon oil spill: A modeling perspective. *Eos Trans. AGU*, 92(6), 45–46. <https://doi.org/10.1029/2011EO060001>
- Lumpkin, R., & Pazos, M. (2007). Measuring surface currents with surface velocity program drifters: The instrument, its data, and some recent results. In A. Griffa, A. D. Kirwan, Jr., A. J. Mariano, T. Özgökmen, & H. T. Rossby (Eds.), *Lagrangian analysis and prediction of coastal and ocean dynamics* (pp. 39–67). Cambridge University Press. <https://doi.org/10.1017/CBO9780511535901.003>
- Luo, H., Bracco, A., Cardona, Y., & McWilliams, J. C. (2016). Submesoscale circulation in the northern Gulf of Mexico: Surface processes and the impact of the freshwater river input. *Ocean Modelling*, 101, 68–82. <https://doi.org/10.1016/j.ocemod.2016.03.003>
- Mahadevan, A., & Tandon, A. (2006). An analysis of mechanisms for submesoscale vertical motion at ocean fronts. *Ocean Modelling*, 14(3–4), 241–256. <https://doi.org/10.1016/j.ocemod.2006.05.006>

- McWilliams, J. C. (2016). Submesoscale currents in the ocean. *Proceedings of the Royal Society A: Mathematical, Physical and Engineering Sciences*, 472(2189), 20160117. <https://doi.org/10.1098/rspa.2016.0117>
- Molemaker, M. J., McWilliams, J. C., & Yavneh, I. (2005). Baroclinic instability and loss of balance. *Journal of Physical Oceanography*, 35(9), 1505–1517. <https://doi.org/10.1175/JPO2770.1>
- Novelli, G., Guigand, C. M., Cousin, C., Ryan, E. H., Laxague, N. J. M., Dai, H., et al. (2017). A biodegradable surface drifter for ocean sampling on a massive scale. *Journal of Atmospheric and Oceanic Technology*, 34(11), 2509–2532. <https://doi.org/10.1175/JTECH-D-17-0055.1>
- Oil slick reaches US coast earlier than expected. (2024). *Oil slick reaches US coast earlier than expected*. Spiegel. Retrieved from <https://www.spiegel.de/panorama/umweltkatastrophe-am-golf-von-mexiko-oelteppich-erreicht-us-kueste-frueher-als-erwartet-a-692171.html>
- Oke, P. R., Allen, J. S., Miller, R. N., Egbert, G. D., & Kosro, P. M. (2002). Assimilation of surface velocity data into a primitive equation coastal ocean model. *Journal of Geophysical Research*, 107(C9). <https://doi.org/10.1029/2000JC000511>
- Olascoaga, M. J. (2010). Isolation on the West Florida Shelf with implications for red tides and pollutant dispersal in the Gulf of Mexico. *Nonlinear Processes in Geophysics*, 17(6), 685–696. <https://doi.org/10.5194/npg-17-685-2010>
- Olascoaga, M. J., & Haller, G. (2012). Forecasting sudden changes in environmental pollution patterns. *Proceedings of the National Academy of Sciences of the United States of America*, 109(13), 4738–4743. <https://doi.org/10.1073/pnas.1118574109>
- Olascoaga, M. J., Rypina, I. I., Brown, M. G., Beron-Vera, F. J., Koçak, H., Brand, L. E., et al. (2006). Persistent transport barrier on the West Florida Shelf. *Geophysical Research Letters*, 33(22), 2006GL027800. <https://doi.org/10.1029/2006GL027800>
- Özgökmen, T. M., Bouffadel, M., Carlson, D. F., Cousin, C., Guigand, C., Haus, B. K., et al. (2018). Technological advances for ocean surface measurements by the consortium for advanced research on transport of hydrocarbons in the environment (CARTHE). *Marine Technology Society Journal*, 52(6), 71–76. <https://doi.org/10.4031/MTSJ.52.6.11>
- Patches of Oil Wash Ashore in Louisiana. (2024). *Patches of oil wash ashore in Louisiana*. Democracy Now. Retrieved from https://www.democracynow.org/2010/5/11/headlines/patches_of_oil_wash_ashore_in_louisiana
- Perez, G. M. P., Vidale, P. L., Klingaman, N. P., & Martin, T. C. M. (2021). Atmospheric convergence zones stemming from large-scale mixing. *Weather and Climate Dynamics*, 2, 475–488. <https://doi.org/10.5194/wcd-2-475-2021>
- Pierrehumbert, R. T. (1991). Large-scale horizontal mixing in planetary atmospheres. *Physics of Fluids A: Fluid Dynamics*, 3(5), 1250–1260. <https://doi.org/10.1063/1.858053>
- Poje, A. C., Özgökmen, T. M., Lipphardt, B. L., Haus, B. K., Ryan, E. H., Haza, A. C., et al. (2014). Submesoscale dispersion in the vicinity of the Deepwater Horizon spill. *Proceedings of the National Academy of Sciences of the United States of America*, 111(35), 12693–12698. <https://doi.org/10.1073/pnas.1402452111>
- Qu, L., Thomas, L. N., Hetland, R. D., & Kobashi, D. (2022). Mixing driven by critical reflection of near-inertial waves over the Texas-Louisiana shelf. *Journal of Physical Oceanography*. <https://doi.org/10.1175/JPO-D-22-0004.1>
- Schlichting, D., Qu, L., Kobashi, D., & Hetland, R. (2023). Quantification of physical and numerical mixing in a coastal ocean model using salinity variance budgets. *Journal of Advances in Modeling Earth Systems*, 15(4), e2022MS003380. <https://doi.org/10.1029/2022MS003380>
- Shadden, S. C., Lekien, F., & Marsden, J. E. (2005). Definition and properties of Lagrangian coherent structures from finite-time Lyapunov exponents in two-dimensional aperiodic flows. *Physica D: Nonlinear Phenomena*, 212(3–4), 271–304. <https://doi.org/10.1016/j.physd.2005.10.007>
- Sinha, A., Balwada, D., Tarshish, N., & Abernathy, R. (2019). Modulation of lateral transport by submesoscale flows and inertia-gravity waves. *Journal of Advances in Modeling Earth Systems*, 11(4), 1039–1065. <https://doi.org/10.1029/2018MS001508>
- Srinivasan, A., Chin, T. M., Chassignet, E. P., Iskandarani, M., & Groves, N. (2022). A statistical interpolation code for ocean analysis and forecasting. *Journal of Atmospheric and Oceanic Technology*, 39(3), 367–386. <https://doi.org/10.1175/JTECH-D-21-0033.1>
- Thomas, L. N., Tandon, A., & Mahadevan, A. (2008). Submesoscale processes and dynamics. In M. W. Hecht & H. Hasumi (Eds.), *Geophysical Monograph Series. American Geophysical Union* (pp. 17–38). <https://doi.org/10.1029/177GM04>
- Thompson, A. F., Lazar, A., Buckingham, C., Naveira Garabato, A. C., Damerell, G. M., & Heywood, K. J. (2016). Open-ocean submesoscale motions: A full seasonal cycle of mixed layer instabilities from Gliders. *Journal of Physical Oceanography*, 46(4), 1285–1307. <https://doi.org/10.1175/JPO-D-15-0170.1>
- Thyng, K. M., Greene, C. A., Hetland, R. D., Zimmerle, H. M., & DiMarco, S. F. (2016). True colors of oceanography. *Oceanography*, 29(3), 10.
- Velissariou, P. (2014). *Gulf of Mexico high-resolution (0.01° × 0.01°) bathymetric grid—Version 2.0, February 2013*. Distributed by: Gulf of Mexico Research Initiative Information and Data Cooperative (GRIIDC), Harte Research Institute, Texas A&M University–Corpus Christi. <https://doi.org/10.7266/N7X63JZ5>
- Waugh, D. W., & Abraham, E. R. (2008). Stirring in the global surface ocean. *Geophysical Research Letters*, 35(20), 2008GL035526. <https://doi.org/10.1029/2008GL035526>
- Wildlife threatened by Oil. (2024). *Wildlife threatened by oil*. NBC News. Retrieved from <https://www.nbcnews.com/slideshow/news/wildlife-threatened-by-oil-36877396>
- Yang, H., Weisberg, R. H., Niiler, P. P., Sturges, W., & Johnson, W. (1999). Lagrangian circulation and forbidden zone on the West Florida Shelf. *Continental Shelf Research*, 19(9), 1221–1245. [https://doi.org/10.1016/S0278-4343\(99\)00021-7](https://doi.org/10.1016/S0278-4343(99)00021-7)
- Yang, Y., McWilliams, J. C., San Liang, X., Zhang, H., Weisberg, R. H., Liu, Y., & Menemenlis, D. (2021). Spatial and Temporal characteristics of the submesoscale energetics in the Gulf of Mexico. *Journal of Physical Oceanography*, 51(2), 475–489. <https://doi.org/10.1175/JPO-D-20-0247.1>
- Zhong, Y., & Bracco, A. (2013). Submesoscale impacts on horizontal and vertical transport in the Gulf of Mexico: Submesoscale transport in Gulf of Mexico. *Journal of Geophysical Research: Oceans*, 118(10), 5651–5668. <https://doi.org/10.1002/jgrc.20402>